Meridional component of oceanic Rossby wave propagation

Roman E. Glazman [a,*], Peter B. Weichman [b]

[a] *Jet Propulsion Laboratory, 4800 Oak Grove Drive, Pasadena, CA 91109, USA*
[b] *BAE Systems, Advanced Information Technologies, 6 New England Executive Park,
Burlington, MA 01803, USA*

Abstract

A three-dimensional spectral analysis of Topex altimeter data reveals a large meridional component k_y of the wavevector $\boldsymbol{k}$ for baroclinic Rossby waves of all timescales. Its existence necessitates some refinements in our estimates of certain basic properties of the Rossby wave field. In particular, by taking into account an actual off-zonal direction of $\boldsymbol{k}$ (often exceeding 70°), one finds that the wavelength, phase speed, and group velocity of mid-latitude Rossby waves (with periods less than 2 years) are much smaller than they appear to be on the assumption of a purely zonal wavenumber vector. Because of a shorter wavelength (yielding kL as high as 0.6, where L is the Rossby radius of deformation), these waves are essentially dispersive. Their group velocity vector may depart from zonal by more than 30°. An important intrinsic feature of the wave spectrum confirmed by our analysis is a broadband distribution with respect to k_y. Some of the dynamical implications of the large k_y/k_x ratio are discussed.
© 2004 Elsevier B.V. All rights reserved.

Keywords: Rossby waves; Satellite altimetry

1. Introduction

Present interest in large-scale oceanic Rossby waves, especially those in the Pacific, was heightened by satellite-based observations (Chelton and Schlax, 1996) showing very

---

* Corresponding author.
 E-mail address: reg@pacific.jpl.nasa.gov (R.E. Glazman).

long (up to thousands of kilometers) baroclinic Rossby waves originating at ocean eastern boundaries and crossing the entire ocean basin. The extremely large wavelength reported in this analysis, making these waves appear non-dispersive, would also imply a purely westward group velocity vector, equal in magnitude to the wave phase speed. As should be expected due to the presence of ubiquitous background currents, the apparent zonal phase speed was found to be at least twice as large as it would be in the absence of background flows. These westward propagating waves are claimed to provide teleconnections between El Niño-Southern-Oscillation (ENSO) events and global weather patterns by influencing ocean gyres and air–sea fluxes in the western Pacific (Chelton and Schlax, 1996). In recent years, Rossby wave motions were found to account for 5–20% of the observed variability in chlorophyll concentration and the latter to be coherent with westward propagating anomalies of sea surface height (SSH) (Cipollini et al., 2001; Uz et al., 2001). The latter studies, along with observations of Rossby wave effects on sea surface temperature (SST) variations (e.g., Hill et al., 2000), provided an independent confirmation of trans-Pacific transport of heat and other quantities at the rate reported by Chelton and Schlax (1996). In addition to the standard analysis of SSH variations in the longitude-time plane at a fixed latitude (used in all the above studies), Cipollini et al. (2000) and Challenor et al. (2001) examined possible deviations from zonal propagation by applying a 3D Radon transform technique to 3D data "cubes" which included a latitudinal dimension. However, due to the intrinsic difficulties of analyzing latitudinal variations—explained in detail in Section 3, and also because the range of off-zonal angles explored by these authors was limited to $\pm 40°$, they did not find significant deviations, and thus confirmed the purely zonal propagation of the Rossby wave phase at all latitudes.

As shown in the present work, the off-zonal deviations of the characteristic wavenumber vector, k, are often well outside the $\pm 40°$ range. As explained in Sections 2 and 3, and confirmed by the data analysis in Section 5, the wavelength and wave speed of mid-latitude Rossby waves (for a given wave frequency) rapidly decrease as k tends to a near meridional orientation. The effect is most important for waves with periods less than 2 years. The existence of a large meridional component of k suggest a more complex view of the Rossby wave field than has emerged in recent years. To advance this view, we explore the full 2D nature of the wave field by using a three-dimensional spectral analysis. One of its features is the separation of the wave field, usually characterized by a very broad range of spatial and time scales, into individual components—namely (near-)semi-annual, (near-)annual, etc., which are clearly identifiable in the 3D spectra. Another important advantage of this analysis is that it permits (as shown in Section 4) extracting information on the meridional structure of the wave field separately for eastward and westward moving disturbances of the SSH field. This "spectral filtering" is crucial because latitudinal variations of the SSH field are too complex (i.e., broad-banded) to be discerned directly from SSH field data.

In most previous studies, the characteristic speeds, wavelengths and frequencies of Rossby waves were inferred from longitude-time plots (also called the "Hovmöller diagrams") of SSH (or SST, or other quantities) variations. In Section 3 we discuss this approach and point out some of its shortcomings. The three-dimensional spectral analysis of Sections 4 and 5 allows one to obviate these shortcomings and explore directional properties of the wave field. This is particularly important in view of the fact that knowledge of the meridional component, k_y, of the wavenumber vector is crucial to test some recent models

of Rossby waves in the presence of ambient flows and topography (see, e.g., Killworth and Blundell, 2003). One inference of our 3D analysis is that the group velocity vector appreciably deviates from the zonal direction, which should lead to a cross-latitudinal transfer of energy, momentum and other quantities, while the trans-Pacific propagation may not necessarily take place. This latter conclusion agrees with the theoretical predictions of Schopf et al. (1981) who studied wave refraction due to the latitudinal dependence of the Rossby radius of deformation *L*. Ocean currents, external forcing, bathymetry and stratification variations may also have considerable influence on Rossby waves in several different ways (e.g., Wang and Koblinsky, 1994; Reznik and Tsybaneva, 1994; Gill, 1982; LeBlond and Mysak, 1978; Killworth et al., 1997; Dewar, 1998; Qiu et al., 1997; Killworth and Blundell, 1999, 2003; Taileux, 2003; Tailleux and McWilliams, 2002). Although we do not specifically discuss these factors, they should be kept in mind when analyzing the spectra reported in Section 5.

Large departures of the baroclinic Rossby wave vector, hence wave phase propagation, from the zonal direction have been known since the 1970s (e.g., Emery and Maggard, 1976; Price and Magaard, 1980; Kang and Magaard, 1980). Price and Magaard showed that in the north Pacific, the meridional component k_y of the wavevector is systematically *much* greater than the zonal component k_x and may be positive as well as negative. The flow pattern in Rossby waves with a near meridional wavenumber vector is characterized by an oscillating near-zonal velocity vector. Among satellite-based studies challenging the idea of a purely westward propagation of Rossby waves, Perigaud and Delecluse (1992) showed that the zonal component of SSH variability is accompanied by an appreciable poleward progression of the wave phase at latitudes above 15°N. Altimeter-based examples of Rossby waves with $\boldsymbol{k}$ deviating from the zonal by more than 45° either poleward or equatorward were presented in Figs. 7 and 8 of Glazman and Cheng (1999).

2. Simple consequences of an anisotropic dispersion

In the absence of background flows, the Rossby wave dispersion law (in polar coordinates) is

$$\omega(\boldsymbol{k}) = -\frac{\beta k \cos(\phi)}{k^2 + L^{-2}}, \tag{1}$$

where $k = (k_x^2 + k_y^2)^{1/2}$ and $\phi = \tan^{-1}(k_y/k_x)$. The physical mechanism responsible for the observed spectrum with a broad range of both positive and negative k_y represents an interesting theoretical topic. While several explanations of the anisotropy of large-scale oceanic eddy turbulence have been proposed in oceangraphic literature, a satisfactory explanation of the anisotropy of the Rossby wave field has proven elusive. Our data analysis suggests that a near-meridional orientation of the wavenumber vector is much more common than zonal orientation. One can easily check (using (1)) that the direction of the group velocity vector $\boldsymbol{V}_g \equiv \nabla_k \omega$; should deviate from zonal by angle ψ related to ϕ via $\tan(\psi) = \sin(2\phi)/[\cos(2\phi) - \varepsilon^{-2}]$, where $\varepsilon \equiv kL$. Although the group velocity of very long, hence non-dispersive, waves ($\varepsilon \to 0$) is indeed westward: $\psi = O(\varepsilon^2)$, we demonstrate in Sec-
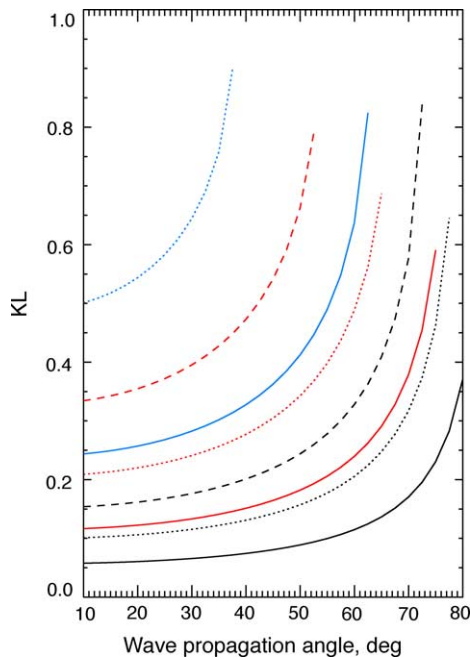
Fig. 1. Non-dimensional wavenumber $\varepsilon = kL$ characterizing Rossby wave dispersiveness with respect to wavelength, as a function of the orientation ϕ of the wavenumber vector, the wave period $T = 2\pi/\omega$, and the geographic latitude θ. Black curves: $T = 2$ years; red curves: $T = 1$ year; blue curves: $T = 1/2$ year; solid curves: $\theta = 15°$ (either north or south); dotted curves: $\theta = 25°$; dashed curves: $\theta = 35°$.

tion 5 that baroclinic Rossby waves at mid-latitudes usually do not satisfy this condition, and ε as large as 0.6 is rather common.

To illustrate the strong dependence of the dispersion parameter ε on the direction ϕ of wave phase propagation, in Fig. 1 we plot ε as a function of ω and ϕ [by solving (1) for k and parameterizing L as $L = c_{klvn}/f(\theta)$, where the Kelvin wave speed is estimated as $c_{klvn} = 3$ m/s and $f(\theta)$ is the latitudinally dependent Coriolis parameter]. This simple calculation demonstrates that even annual and biennial Rossby waves become rather dispersive given sufficiently large values of ϕ.

As the wavelength becomes shorter, the degree of the wave nonlinearity increases (this intuitive conclusion can be reached formally by scaling the terms in the potential vorticity conservation equation). This effect has a remote analogy in the shoaling of surface gravity waves as they approach the beach, which leads to wave steepening.

Finally, we note the effect of a large k_y on the Doppler shift $\boldsymbol{k} \cdot \boldsymbol{U}$ created by a uniform background current $\boldsymbol{U}$ (see, e.g., Gill, 1982). Provided the intrinsic wave frequency ω is very low, even a very small Doppler shift (such as caused by a 1 cm/s mean current) will appreciably affect the observed frequency. Due to the strong inequality $k_y \gg k_x$, the zonal and meridional components of $\boldsymbol{U}$ may produce comparable contributions to ω_{obs}, although in most ocean regions U_y is much smaller than U_x. For the range of k_x and k_y in our data analysis, a concrete example is illustrated in Section 5. Of course, for a more realistic description of

currents' influence one must account for variations of a current field in both space and time, on scales comparable to or shorter than the scales of Rossby waves themselves. A detailed treatment for a case of vertically varying (baroclinic) currents is presented in Killworth et al. (1997). Further studies include Qiu et al. (1997), Dewar (1998).

3. Limitations of lon-time and lat-time plots

The great usefulness of the Hovmöller diagrams is well known. However, like most other techniques, this approach (and the similar latitude-time plots) has its shortcomings. Let us consider separately the limitations arising due to a non-zonal propagation of ocean waves and those due to multiple-scale variability of oceanographic fields.

In the lon-time plots of SSH, wave motions manifest themselves as elongated features whose tilt depends on the zonal speed of the wave phase propagation:

$$\tilde{C}_x = \frac{\omega_{\text{obs}}}{k_x} = -\frac{\beta L^2}{1 + \varepsilon^2} \tag{2}$$

where ω_{obs} is the observed wave frequency, and the last equality follows from (1). For a purely zonal propagation (i.e., $k_x \equiv k$) and in the absence of background currents, this apparent speed $\tilde{C}_x$ represents the *true intrinsic phase speed*: $\tilde{C}_x = c \equiv \omega/k$. The apparent wavelength L_x and frequency inferred from the lon-time plots also represent intrinsic wave properties in this case. If, however, the actual wavevector is not zonal, the apparent wavelength $L_x = \lambda/\cos(\phi)$ inferred from the lon-time plots may differ dramatically from the true wavelength λ. The apparent zonal phase speed $\tilde{C}_x$ is useful for testing the Rossby wave dispersion law (1) (divided by k_x)—as was done by Chelton and Schlax (1996) and by later authors. However, given a large angle ϕ, this quantity also is far from both the actual phase speed c and, more importantly, from the zonal component of the group velocity vector V_g. The latter for non-dispersive waves would be strictly westward and equal to βL^2, whereas V_g of dispersive waves may be away from zonal by more than $30°$ (for annual and shorter-period waves) and its magnitude is $V_g = \beta L^2 \hat{v}(\varepsilon, \phi)$, where

$$\hat{v}(\varepsilon, \phi) = \frac{\sqrt{1 - 2\varepsilon^2 \cos(2\phi) + \varepsilon^4}}{(1 + \varepsilon^2)^2}. \tag{3}$$

For $\varepsilon \geq 0.5$ one obtains $\hat{v} \approx 0.5$ or less: see Fig. 2. Such a significant decrease in the group velocity has important implications. One of them relates to the Pacific Transit Time [estimated in Chelton and Schlax (1996) to be 2.5–35 years at latitudes 10–35°, respectively]. Apparently, this time is not only underestimated by using an exaggerated wave speed but may be meaningless because dispersive Rossby waves, deviating from the zonal direction, will not necessarily traverse the entire Pacific from east to west.

One more limitation of the Hovmöller diagrams stems from a rather weak dependence of $\tilde{C}_x(\omega)$ in (2) on both ω and ϕ. As a result, Rossby waves with different (even opposing) meridional components and different frequencies appear almost indistinguishable in these plots. In the absence of information on the meridional component k_y, accurate estimation of wave properties becomes, in general, impossible.
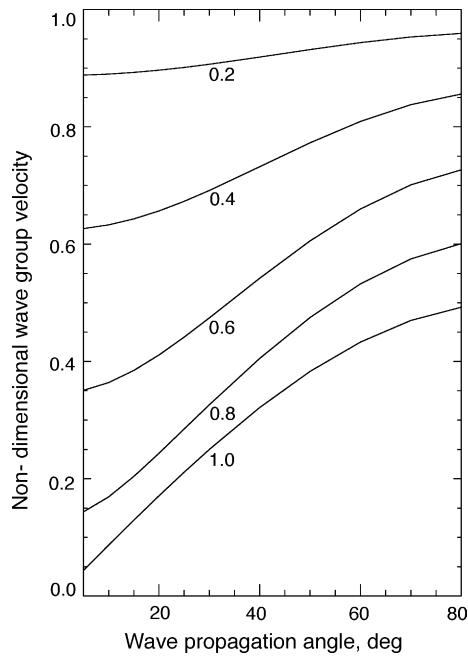
Fig. 2. Non-dimensional group velocity, $\hat{v}(\varepsilon, \phi)$, given by Eq. (3), as a function of phase propagation direction ϕ and dispersion parameter $\varepsilon = kL$ (indicated next to the curves).

Unfortunately, complementing the lon-time plots with lat-time diagrams, as was attempted by Cipollini et al. (2000), does not help determining the full wavenumber vector. The lat-time plots do not show a pattern of tilted ridges and troughs so apparent in the lon-time plots. This is because the superposition of simultaneous equatorward and poleward motions in the Rossby wave field creates a noise-like interference pattern which is further complicated by the fact that the apparent meridional phase speed $\tilde{C}_y = \omega/k_y = -\beta L^2 \cot(\phi)/(1 + \varepsilon^2)$ of each wave system depends on the propagation angle φ. This is one of the reasons why the 3D Radon transform technique (Challenor et al., 2001) fails to reveal the meridional component.

4. Data analysis approach

For a broad-banded multi-directional SSH field, many of the above difficulties can be avoided if the characteristic wavenumbers, wave frequencies and wave speeds are determined separately for each wave system. The latter are associated with individual peaks in a three-dimensional spectrum of SSH variations. To implement this approach, we shall employ a high-resolution statistical technique of 3D autocorrelation and spectral analysis of irregularly spaced and gappy satellite data (Glazman et al., 1996a).

The size of ocean areas selected for spectral analysis is chosen as a compromise between the need to reduce effects of spatial non-stationarity of the Rossby wave field and the need

to sample SSH variations on scales over which the SSH field varies as a wave passes through the area—i.e., about half the typical wavelength. According to Fig. 1, typical wavelengths of annual and shorter-timescale Rossby waves at mid-latitudes are under 10^3 km. Therefore, the latter requirement can be satisfied by selecting a $10° \times 10°$ area. However, the spatial stationarity requirement is only barely satisfied on this scale because the Rossby radius of deformation (hence, wave field properties) changes by nearly 50% between two latitudes $10°$ apart. We have carried out trial estimates for different ocean areas with linear dimensions from 500 to 3000 km and came to the conclusion that $10° \times 10°$ boxes provide the best compromise, at least for Rossby waves with periods under 2 years. Spectral properties of multi-annual and low-latitude Rossby waves, whose typical wavelengths exceed 10^3 km, will not be accurately estimated using such boxes.

Although of course they have their own limitations, as, e.g., discussed in Glazman et al. (1996a), Monin and Yaglom (1980), Fourier techniques appear to be well suited for analysis of random processes characterized by multiple-scale variability. To be able to analyze a set of irregularly spaced and gappy data, we first estimate a spatio-temporal autocorrelation function for a given ocean region

$$W(\boldsymbol{r}, \tau) = \langle \zeta(\boldsymbol{x}, t)\zeta(\boldsymbol{x} + \boldsymbol{r}, t + \tau) \rangle \tag{4}$$

by averaging SSH products with similar space and time lags, $\boldsymbol{r}$ and τ, over the entire dataset. Since this approach was described in great detail in earlier work, we shall reiterate only a few important points. SSH measurements $\zeta(\boldsymbol{x}, t)$ and $\zeta(\boldsymbol{x}', t')$ employed to ultimately produce an estimate of $W(\boldsymbol{r}, \tau)$ at an individual point (r_x, r_y, τ) are never taken from the same satellite pass. Rather, they belong not only to different passes (at least 7 days apart) but also to different ground tracks intersecting the selected $10° \times 10°$ area. This procedure results in a dense coverage of the $(\boldsymbol{r}, \tau)$ space. Specifically, the characteristic number of SSH pairs falling into each bin (of size 40 km $\times$ 40 km $\times$ 7 days) of the $(\boldsymbol{r}, \tau)$ space varies between 10^3 and 10^4 depending on the time interval of Topex data used in analysis. The gridding of the original data onto a uniform mesh is thus unnecessary, and the results do not reveal any systematic bias due to the configuration (such as the orbit inclination) of the satellite tracks.

Application of spectral windows in the Fourier transform of (4) increases the number of degrees of freedom (by three to eight times) and further suppresses adverse effects of a limited area and of the field's spatial and temporal non-stationarity (see, e.g., Jenkins and Watts, 1968). A trade-off of using the spectral windowing is a widening of individual spectral peaks. The full 3D spectrum is thus given by (the real part of):

$$F_3(\omega, \boldsymbol{k}) = \frac{1}{(2\pi)^3} \int \mathrm{d}^2\boldsymbol{r} \int \mathrm{d}\tau W(\boldsymbol{r}, \tau) H(\boldsymbol{r}, \tau) \mathrm{e}^{\mathrm{i}(\boldsymbol{k} \cdot \boldsymbol{r} - \omega\tau)}, \tag{5}$$

where the even function $H(\boldsymbol{r}, \tau)$ (for example, the Hanning window) tapers off to zero as the lags approach their maximal values. The effectiveness of this approach has been demonstrated in several applications (Glazman et al., 1996b; Glazman and Cheng, 1999; Weichman and Glazman, 2002) and its error analysis is provided in Glazman et al. (1996a). Since this analysis yields only a crude upper bound on the error, an additional, purely empirical analysis was also conducted in Glazman et al. (1996a), as well as in the present work,

to estimate actual errors. This was accomplished by generating a (Gaussian) random field with a specified spectrum and then applying the present method to individual realizations of this simulated field. Spectral estimates of the simulated field were then compared to the original spectrum. For 3-year long series of field observations over $10° \times 10°$ ocean areas, the spectra differed by not more than 20%.

One of the main advantages of the present approach is that no aliasing of energy from one subrange to another occurs because no Fourier expansion of the observed field is carried out. This of course is achieved at the cost of computational efficiency. For instance, computing a 3D autocorrelation function and its Fourier transform for a 3-year period of Topex observations in a single region, using a 0.5 GHz CPU on a Linux PC, takes up to 24 h.

Fig. 5 illustrates a 3D spectrum estimated for Region A (see the map in Fig. 3) for a 3-year period of SSH observations. This plot shows an *iso*-surface of spectral density for an arbitrary value chosen for best visual effect. A much more quantitative illustration of this and other spectra is given in Figs. 6–10 (discussed in Section 5) using contour plots of 2D spectra obtained by integrating $F_3(\omega, k)$ over one of the axes.

Once $F_3(\omega, k)$ has been obtained, various physical quantities can be estimated by computing appropriate spectral moments. For example, the meridional component of the fundamental phase velocity vector c for Rossby waves in a given frequency range is estimated as a spectrum-weighted $c_y(k, \omega)$. The latter quantity is given by the second term in the standard definition of vector c (Pedlosky, 1979; LeBlond and Mysak, 1978; Phillips, 1977; Witham, 1974):

$$c \equiv \frac{\omega}{k} k = \hat{i} \left(\frac{k_x}{k} \right) \left(\frac{\omega}{k} \right) + \hat{j} \left(\frac{k_y}{k} \right) \left(\frac{\omega}{k} \right), \tag{6}$$
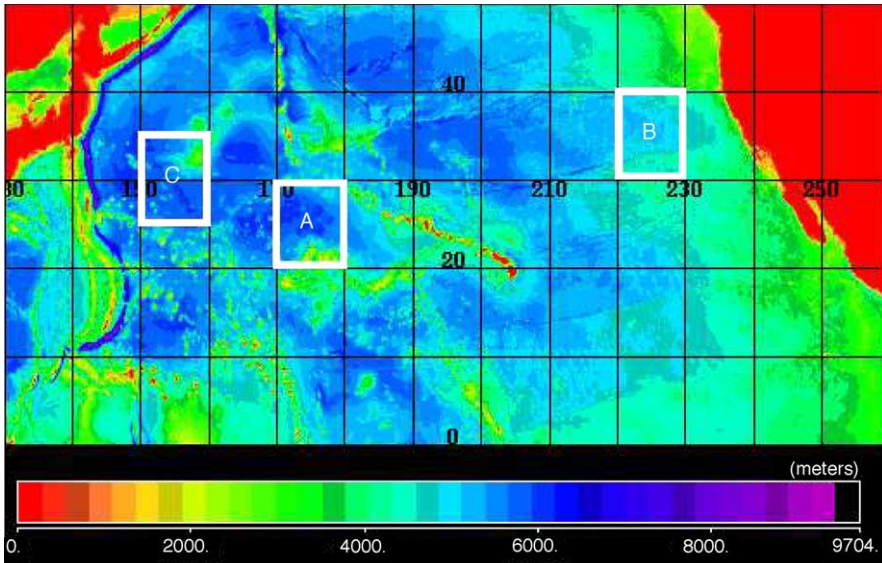

Fig. 3. Regions of the North Pacific selected for SSH data analysis. Color scale represents ocean depth.

where $\hat{i}$ and $\hat{j}$ are orthogonal unit vectors. Therefore, the characteristic value of c_y for the frequency range (Ω_1, Ω_2) is given by

$$\bar{c}_y = \frac{1}{\sigma_1^2} \int_{\Omega_1}^{\Omega_2} d\omega \int_{K_{x,0}}^{K_{x,1}} dk_x \int_{K_{y,0}}^{K_{y,1}} dk_y \frac{\omega k_y}{k^2} F_3(\omega, k_x, k_y). \tag{7}$$

Here $(K_{x,0}, K_{x,1})$ is the wavenumber range corresponding to westward propagating waves, and $(K_{y,0}, K_{y,1})$ is the appropriate range of meridional wavenumbers—either all positive (for northward propagation) or all negative (for southward propagation). Thus, the integration limits serve to specify the range of scales and propagation directions to be considered. The normalization constant σ_1^2 (given by the same integral but with the $\omega k_y/k^2$ factor omitted) represents the SSH variance for the given range of frequencies and wavenumbers. Similarly, the characteristic meridional wavenumber $\bar{k}_y$ is found from (7) by replacing $c_y(\mathbf{k}, \omega)$ by k_y. The zonal component, $\bar{c}_x$, of the phase velocity vector (either westward or eastward), the zonal phase speed $\tilde{C}_x$, and the mean zonal wavevector component $\bar{k}_x$, or some other properties of the wave field, are estimated in a similar way.

In order to assess both the interannual variability and the "climatology" of the SSH field, we use 3-year subsets of a 9-year dataset of Topex data as well as the full 9-year dataset. The former yields statistically significant information on oceanic motions occurring within a given time interval, which include yearly and shorter timescales, while the latter contains also statistically significant spectral estimates for interannual scales. We shall present results only for three regions, shown in Fig. 3. These regions along with additional computations (some of which presented in Table 2) cover a rather diverse set of ocean conditions to support our final conclusions presented in Section 6.

SE	NW
SW	NE

SE	NW
NE	SW

Fig. 4. Key to the asymmetric spectra in Figs. 7–10: Each quadrant in the corresponding panels of those diagrams contains information about wave systems propagating in the directions marked here as NW, SW, etc.

In the next section we shall use various two-dimensional spectra $F_2(\omega, k_{x,y})$ obtained either by integrating the full 3D spectrum over positive k_y or over positive k_x values. This kind of half-space integration yields asymmetric 2D spectra (see, e.g., Fig. 7, discussed in Section 5 below) whose interpretation is facilitated by the diagram in Fig. 4. The top panel of this diagram shows the dominant directions of wave propagation for wave systems associated with the spectral peaks appearing in the corresponding quadrants of the top panel of Fig. 7. For instance, the peak labelled 'b' in the top panel of Fig. 7 is due mainly to waves propagating in the SW direction. This particular wave system manifests itself in the second quadrant of the bottom panel of Fig. 7, which becomes obvious due to the fact that this is the only well pronounced spectral peak corresponding to the characteristic frequency of about 0.026 rad/day. A much smaller peak at the same frequency is noticeable in the first quadrant of the bottom panel indicating the existence of a very weak NW system.

The spectral filtering used to produce Figs. 7–10 is somewhat tentative because of an insufficient accuracy of 3D spectra at low frequencies/wavenumbers. This fundamental limitation (encountered in spectral analysis of almost all geophysical fields) is due to the fact that the temporal and spatial extent of an observational domain is inevitably limited and the observed fields are neither strictly (statistically) stationary nor spatially homogeneous on large scales (Monin and Yaglom, 1980). Nevertheless, our estimates remain approximately valid for timescales shorter than the observation period and for spatial scales within the linear dimensions of the ocean regions.

The asymmetric spectra allow quick estimates of spatial scales L_x, L_y and dominant wave frequency $\bar{\omega}$ for each $(\omega, \boldsymbol{k})$ subrange (hence, wave system) of interest. As mentioned in Section 2, these quantities yield the full velocity vector and wavelength.

5. Analysis for selected regions

Figs. 5–7 describe a relatively simple situation observed in region 'A' during a 3-year period commencing 1 March 1993. The 2D spectra $F_2(\omega, k_x)$ and $F_2(\omega, k_y)$, obtained by integrating the 3D spectrum $F_3(\omega, \boldsymbol{k})$ over the entire ranges of k_y and k_x, respectively, are shown in Fig. 6. Since the integration intervals include both positive and negative k_y and k_x, the top panel of Fig. 6 characterizes zonal propagation of all types of QG motions, including Rossby waves whose meridional components may be either poleward or equatorward. The dominance of westward propagation for all timescales is obvious by comparing the two panels of Fig. 5. This is also evident in Fig. 6 that shows most of the energy in the first quadrant of the (ω, k_x) plane (let us recall that due to central symmetry of these spectra, the first and third quadrants are equivalent). The bottom panel of Fig. 6 describes meridional propagation of all types of slow motions including both westward and eastward systems. Apparently, the three main peaks, 'a', 'b', and 'c' found in the top panel correspond to four spectral peaks in the bottom panel. The wave system 'a' contains two components—one southward and one northward.

A more instructive plot, Fig. 7, is obtained by integrating the 3D spectrum only over positive k_y (top panel) or positive k_x (bottom panel) starting at wavenumbers greater than about $2\pi/2000$ rad/km. As a result of this spectral filtering, the central symmetry is broken, and the first quadrant in the top panel is dominated by westward waves whose meridional
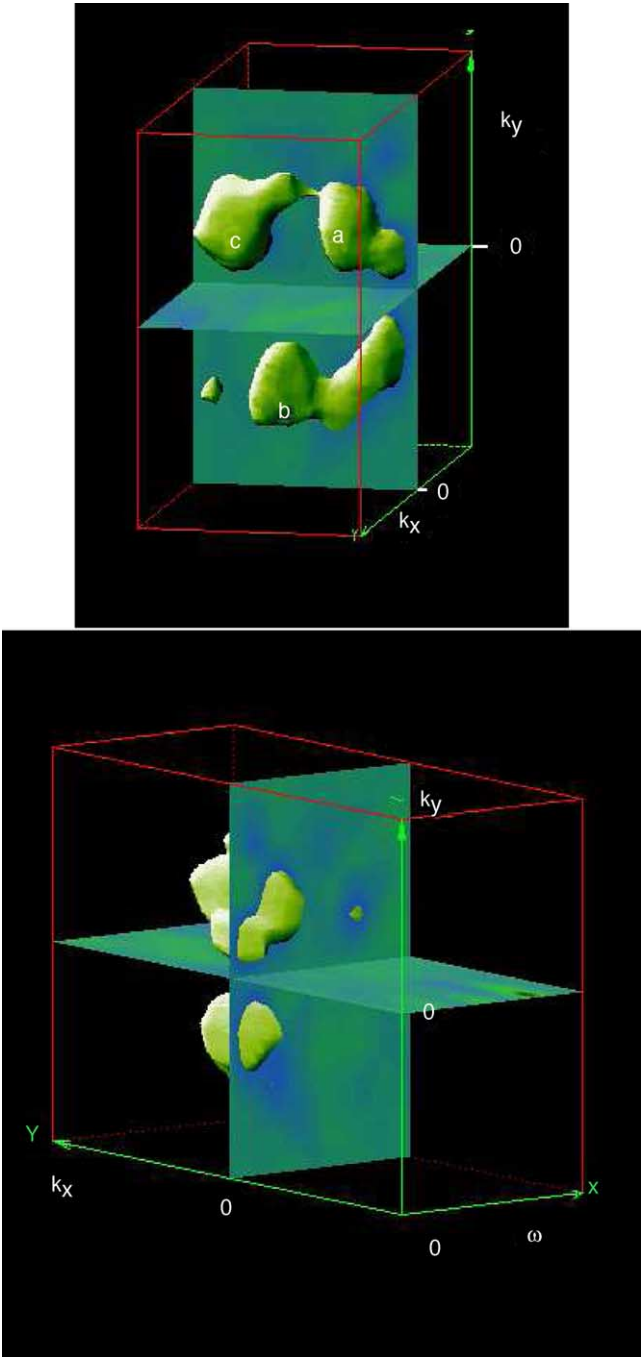
Fig. 5. An *iso*-surface of spectral density $F_3(\omega, \boldsymbol{k})$ for region A, corresponding to Figs. 6 and 7. Top panel gives a view of the $k_x \geq 0$ sub-space of the $\omega \geq 0$ half-space, and the bottom panel shows the $k_x \leq 0$ sub-space.
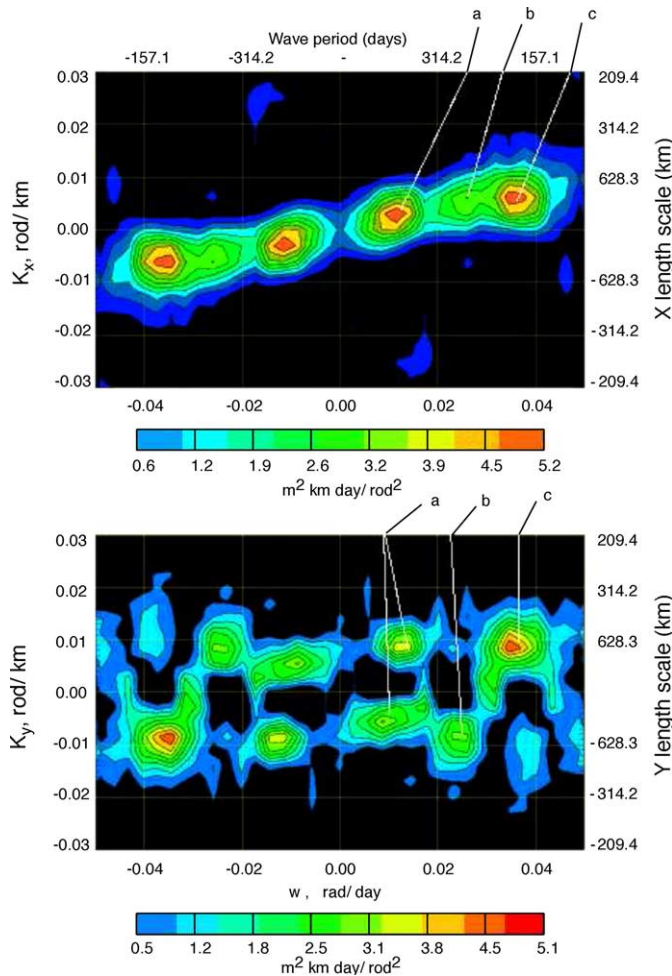
Fig. 6. SSH spectra for region A, based on Topex observations in the period 1 March 1993 to 1 March 1996. Top panel: $F_2(\omega, k_x)$ obtained by integrating the full 3D spectrum $F_3(\omega, \boldsymbol{k})$ over the entire range of k_y. Bottom panel: $F_2(\omega, k_y)$ obtained by integrating the 3D spectrum over all k_x.

component is northward. Fig. 4 facilitates the interpretation of these spectra, while the identification of corresponding peaks between top and bottom diagrams of Fig. 7 is based on their dominant frequencies.

The meridional component of all signals can be inferred from the bottom panel of Fig. 7. Its right half (i.e., the semi-plane $\omega > 0$) shows three main peaks, two of which ($k_y > 0$) represent northwest signals, and one ($k_y < 0$) southwest. The left half ($\omega < 0$) contains eastward moving systems. Thus, a low-energy peak in the fourth quadrant represents a very weak system propagating southeast.

Numerical estimates of wave speeds, directions and wavelengths for each wave system, as described in Section 4, are rather close to the numbers that can be easily inferred directly
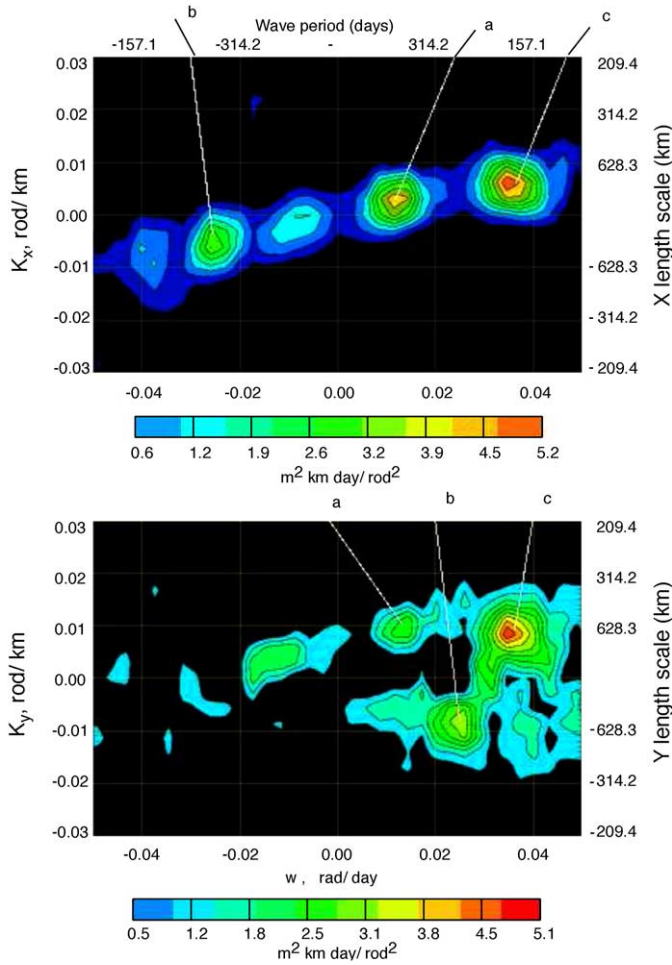
Fig. 7. Same as Fig. 6 except that the range of k_x and k_y over which the 3D spectrum was integrated is limited to positive values as explained in the text.

from the plots. Table 1 lists characteristic frequencies and wavenumber components for each identifiable system. The corresponding wavelength λ and wave period T are also provided. Assuming the Rossby radius of deformation for this region to be $L = 53$ km, we estimate the dispersion parameter $\varepsilon = \bar{k}L$ for each spectral peak. The direction ϕ of the wavenumber vector is found as $\tan^{-1}(\bar{k}_y/\bar{k}_x)$. With these values we then evaluate the intrinsic non-dimensional group velocity, Eq. (3), that would be observed in the absence of background flows. The intrinsic (dimensional) group speed of non-dispersive waves in this ocean region would be $\beta L^2 \approx 5.8$ cm/s. As demonstrated in Table 1, the wave dispersion leads to a 30–50% reduction of this speed.

The last two columns of Table 1 present observed values of the apparent zonal phase speed $\tilde{C}_x = \omega/k_x$ and of the actual phase speed $c = \omega/k$. Evidently, at mid-latitudes, $\tilde{C}_x$ agrees

Table 1
Characteristic parameters of wave systems observed in regions A–C

ω (rad/day)	k_x (rad/km)	k_y (rad/km)	λ (km)	T (months)	ε	ϕ (°)	V_g	$\tilde{C}_x$ (cm/s)	c (cm/s)
Region A (lat: 25°N; $L=53$ km; $\beta L^2 = 5.8$ cm/s)									
Figs. 6 and 7									
0.01	0	0.01	658	16.1	0.51	70.4	0.79	4.7	1.6
0.03	0.01	−0.01	650	7.7	0.51	−50.9	0.49	5.1	3.2
0.03	0.01	0.01	572	6.1	0.58	52.4	0.66	5.9	3.6
Fig. 8									
0.01	0	−0.01	621	29.9	0.54	−81.5	0.51	5.4	0.8
0.02	0	−0.01	504	12.2	0.66	−74.2	0.3	5.9	1.6
0.03	0	0.01	738	7.6	0.45	56.5	0.81	6.8	3.8
0.04	0.01	−0.01	483	6.0	0.69	−67.4	0.31	8.1	3.1
Region B (lat: 35°N; $L=32$ km; $\beta L^2 = 1.9$ cm/s)									
Fig. 9									
0.01	0	0.01	524	17.0	0.38	66.4	0.87	3.0	1.2
0.01	0.01	−0.01	370	15.6	0.54	−58.7	0.76	1.8	0.9
0.02	0.01	0.02	345	9.5	0.58	68.8	0.74	3.9	1.4
Region C (lat: 30°N; $L=45$ km; $\beta L^2 = 4.0$ cm/s)									
Fig. 10									
0.01	0	0	1377	38.1	0.21	−64.0	0.91	3.2	1.4
0.01	0	0.01	532	23.3	0.53	90.0	0.77		0.9
0.01	0	0.01	602	17.5	0.47	73.3	0.57	4.6	1.3
0.02	0	0	1635	13.1	0.17	−38.7	0.92	6.2	4.8
0.02	0	0.01	467	11.6	0.61	74.9	0.69	6.0	1.5
0.03	0	0	1460	7.9	0.19	−30.7	0.96	8.3	7.1
0.03	0.01	−0.01	562	6.5	0.50	−63.4	0.49	7.4	3.3
0.05	0.01	−0.01	658	4.6	0.43	−47.1	0.83	8.2	5.6

Central latitudes, baroclinic Rossby radii of deformation, and characteristic group speeds (assuming non-dispersive regime of Rossby waves) are provided.

Table 2
Characteristic wave number vectors estimated for select ocean regions (of varying size) over time intervals ranging from 3 to 9 years

Region boundaries		Characteristic wave vectors of (near-)annual Rossby waves		Characteristic wave vectors of (near-)semi-annual Rossby waves	
East–west (°)	South–north (°)	k_x (rad/km)	k_y (rad/km)	k_x (rad/km)	k_y (rad/km)
220–240	15–25			7.00E−003	1.30E−002
180–200	15–25	2.00E−003	1.30E−002		
180–200	15–25	2.00E−003	−4.00E−003		
180–200	15–25	3.50E−003	−1.20E−002		
230–260	25S–15S	2.60E−003	8.00E−003		
210–245	15–25	1.50E−003	−7.00E−003		
160–170	20–30	4.00E−004	−1.20E−002	5.00E−003	1.20E−002
210–220	30–40			1.20E−002	−4.00E−003
210–220	20–25	3.50E−003	0		

with the corresponding quantity reported in Chelton and Schlax (1996), which confirms its sensitivity to ambient mean currents. However, it is also interesting that the actual phase speed c is less sensitive to ambient flows. Accounting for the observed ϕ, this speed is in reasonable agreement with Fig. 11, which represents Eq. (1) cast in the form $c(\omega, \phi) = \omega/k(\omega, \phi)$, where $k(\omega, \phi)$ is a functional inverse of (1). Since at latitudes below 30°, the relative influence of β on c is negligible compared to that of L, we used a constant value of β (corresponding to a 25° latitude) to produce Fig. 11.

Although there are many interesting features in Figs. 6 and 7, we shall confine our attention to long (greater than 200 km) Rossby waves with periods greater than 4 months. The three largest peaks at $\omega > 0$ in the two panels of Fig. 7 fall in this category. Therefore, our
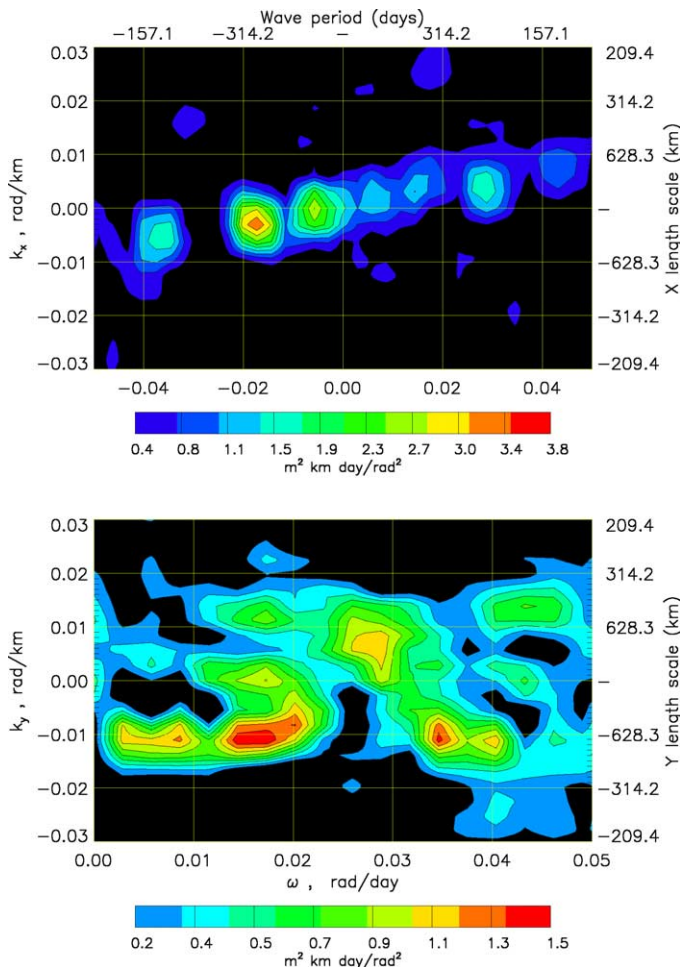

Fig. 8. 2D spectra for region A, analogous to Fig. 7 but for the 3-year period starting 1 March 1999, and only for positive ω.

subsequent bottom-panel plots will show only the $\omega > 0$ half-plane. Since the magnitudes of k_y for these spectral peaks are significantly greater than k_x, the phase velocity vectors always depart from the zonal direction by more than $45°$.

Similar plots for the next 3-year interval (not presented) show that the meridional component of the 1.5-year waves is negligibly small and the waves are close to purely zonal. However in the period starting 30 March 1999 (see Fig. 8), southward motions dominate. The annual and longer period waves depart from the westward direction by more than $70°$. Likewise, the phases of shorter period waves propagate southwest as well as northwest at angles well in excess of $45°$.

In Fig. 9 we illustrate QG dynamics in the eastern North Pacific region 'B' for the 9-year period beginning 1 March 1993. These plots are obtained in the same fashion as Fig. 7.
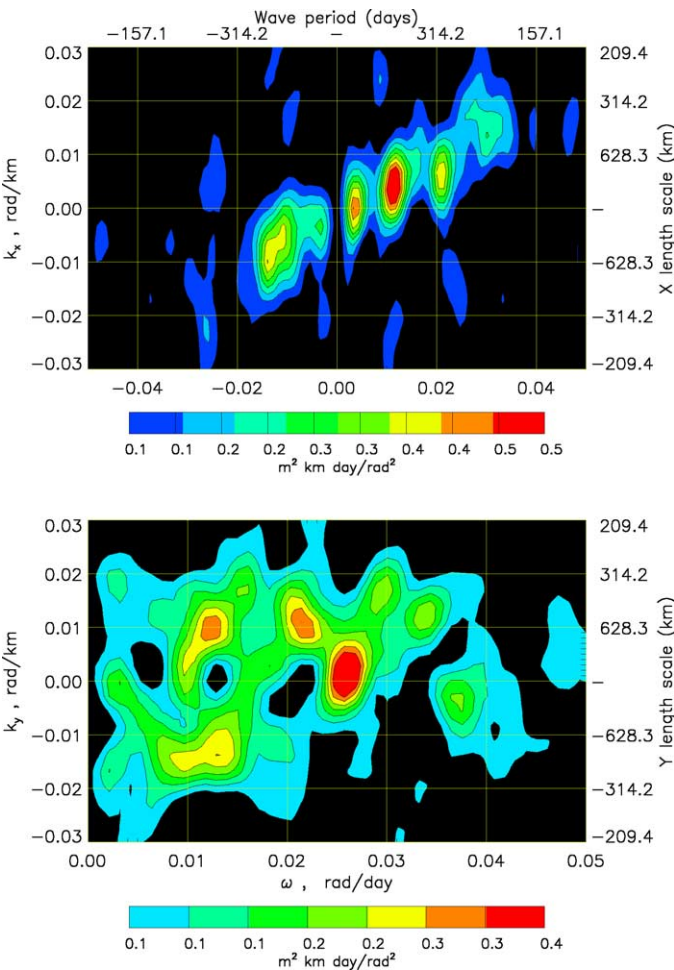

Fig. 9. 2D spectra for region B, analogous to Fig. 8 but for the 9-year period starting 1 March 1993.

The top panel indicates that the motions are predominantly northwest, and the bottom panel reveals a variety of wave systems of which only the waves with a near 8-month period are dominated by a zonally propagating component. All other systems depart from the zonal direction by more than 45°. Quantitative results for some of the spectral peaks are summarized in Table 1. Our analysis of 3-year subsets of this dataset shows again a large interannual variability of wave directions with the characteristic values of ϕ varying from $-60°$ to $+72°$.

Finally, in Fig. 10 we present results for the western end of the North Pacific (region 'C' in Fig. 3) for 9 years of Topex data. It is no surprise that this dynamically rich area contains a great variety of motions with timescales up to the length of the observation period. All spectral peaks in this figure point to the presence of appreciable meridional components:
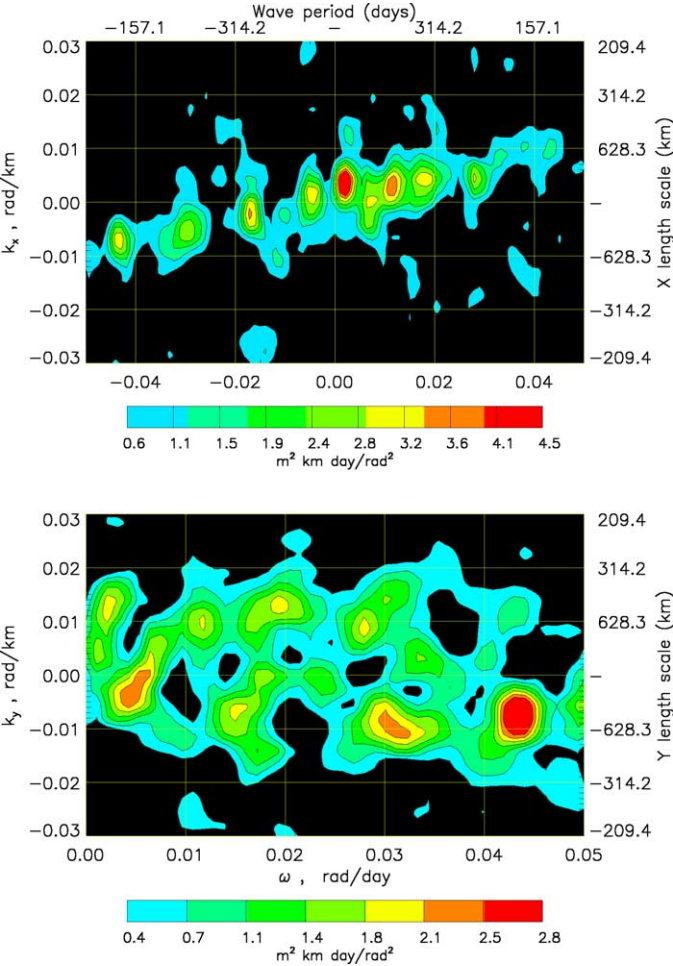

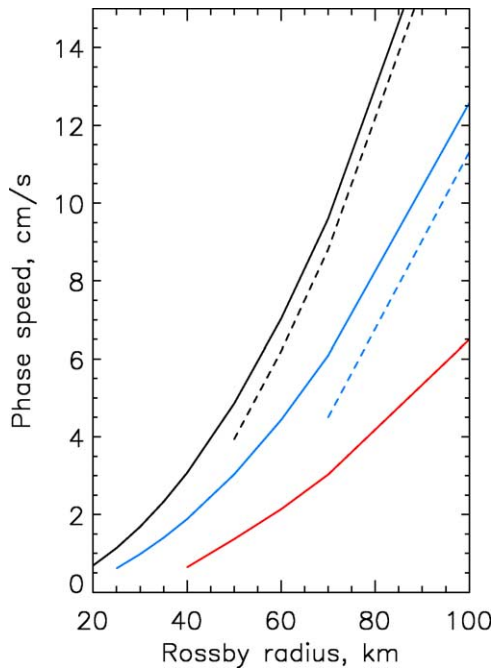Fig. 10. The 2D spectra for region C, analogous to Fig. 8.

Fig. 11. Phase speed c of Rossby waves as a function of Rossby radius of deformation L. Solid curves: annual-period waves; dashed curves: semi-annual waves. Black curves: $\phi = 0°$; blue curves: $\phi = 50°$; red curves: $\phi = 70°$. The truncation of the curves at smaller L, as well as the absence of the red dashed curve, are consequences of the fundamental limit on the intrinsic frequency of Rossby waves at a given latitude as explained in the text.

$k_y \gg k_x$, hence $k \gg k_x$. All these wave systems are dispersive with the typical values of $kL \approx 0.5$. However, due to strong currents and intense mesoscale processes occurring in this region, these wave motions are probably coupled with local dynamics. Therefore, quantitative analysis of Fig. 10 (which is beyond the scope of the present paper) would require much more elaborate tools than the linear wave dispersion law (1).

Many of the features in Figs. 9 and 10 can be better understood by performing spectral analysis on several small subsets of the data, such as 2- or 3-year intervals. This analysis reveals interannual variability of wave properties: in some periods the motions are dominated by northwest waves and in others by southwest. This explains why the spectra computed from long time series, such as Figs. 9 and 10, often contain both southward and northward wave systems.

The characteristic wave frequencies presented in Table 1 rarely correspond to exactly semi-annual, annual, or biennial oscillations. These variations of the observed frequencies may be related not only to the natural variability of external forcing, but also to the Doppler shift caused by mean ambient currents. Let us, for example, allow for a constant mean drift of just 1 cm/s for the zonal component (only), and assume $k_x \approx 0.005$ rad/km. The Doppler shift $\Delta\omega = k_x U_x$ in this case would make annual Rossby waves appear as 9-month period waves. The data on ocean current climatology, for example, available in the ECCO (Esti-

mating the Circulation and Climate of the Ocean) website: http://www.ecco-group.org/las which provides live data access, indicate that at depth below, say, 190 m, characteristic zonal currents in region A are about 1.5 cm/s and meridional component is about 0.2 cm/s. Therefore, a Doppler shift may well be a factor influencing the observed wave frequencies and wave speeds.

Although our illustrations, Figs. 5–10, represent only three ocean regions, the analysis described in this section has been carried out for many other regions of the World Ocean. Some of these results are listed in Table 2. All such results are consistent with the above findings that baroclinic Rossby waves tend to have a relatively large meridional component of the wavenumber vector which may be either poleward or equatorward. These waves are shorter than would appear from the longitude-time plots, and are rather dispersive (i.e., $kL \approx 0.4$–0.7).

6. Conclusions

While nearly zonal propagation of Rossby waves does occur sometimes in some regions, typical directions of the characteristic wavenumber vector deviate from the zonal by 50–80°, either poleward or equatorward. These deviations are natural for Rossby waves due to the anisotropy of the wave dispersion. A poleward decrease of the Rossby radius of deformation, hence of the intrinsic wave speed (Fig. 11), provides an additional cause of a poleward deflection of the wave propagation—through refraction.

The strong deviations of the wave vector from zonal are responsible for a considerable decrease of the actual wavelength and, hence, of both the phase speed c and the group velocity V_g from values for these quantities that would be inferred from longitude-time plots on the assumption of zonal propagation. Our data analysis highlights the essentially dispersive nature of mid-latitude baroclinic Rossby waves with wave periods up to 2 years, whereas analysis based on the Hovmöller diagrams completely misses this important aspect.

The existence of an appreciable meridional component of V_g has important dynamical consequences and it must be allowed for in ocean models. However, this fact is not always appreciated, and the notion of Rossby waves as travelling strictly westward is often used as the basis for simplified models of the Rossby wave field. One such model (expressing the conservation of potential vorticity on a beta plane) is

$$\partial_t(\partial_{xx} - L^{-2})\eta + \beta\partial_x\eta = F, \tag{8}$$

where η is usually the thermocline vertical displacement from its mean depth, F is the external forcing function, and β and L are the beta parameter and Rossby radius of deformation, respectively. Apparently, this equation is valid only when $k_x^2 \gg k_y^2$. If Rossby waves were indeed purely zonal, their wavelength would, in most cases, be sufficiently large to justify an even more drastic simplification, namely the neglect of the entire wave dispersion term $\Delta\eta$ in (8), leading to a very popular equation $\partial_t\eta + c\partial_x\eta = F$. The fact that k_y is at least of the same order as, and often much greater than, k_x makes such one-dimensional models generally inadequate.

Acknowledgements

References

Challenor, P.G., Cipollini, P., Cromwell, D., 2001. Use of the 3D Radon transform to examine the properties of Rossby waves. J. Atm. Ocean Technol. 18, 1558–1566.

Chelton, D.B., Schlax, M.G., 1996. Global observations of oceanic Rossby waves. Science 272, 234–238.

Cipollini, P., Cromwell, D., Challenor, P.G., Raffaglio, S., 2001. Rossby waves detected in global ocean colour data. Geophys. Res. Lett. 20 (2), 323–326.

Cipollini, P., Cromwell, D., Quartly, G., Challenor, P.G., 2000. Remote sensing of oceanic extra-tropical Rossby waves. In: Halpern, D. (Ed.), Satellites, Oceanography and Society. Elsevier, Amsterdam, pp. 99–123.

Dewar, W., 1998. On too-fast baroclinic planetary waves in the general circulation. J. Phys. Oceanogr. 28, 1739–1758.

Emery, W.J., Maggard, L., 1976. Baroclinic Rossby waves as inferred from temperature fluctuations in the eastern Pacific. J. Mar. Res. 34, 365–385.

Gill, A.E., 1982. Atmosphere–Ocean Dynamics. Academic Press, New York, p. 662.

Glazman, R.E., Cheng, B., 1999. Altimeter observations of baroclinic oceanic inertia-gravity wave turbulence. Proc. R. Soc. Ser. A 455, 91–123.

Glazman, R.E., Fabrikant, A., Greysukh, A., 1996a. Statistics of spatio-temporal variations of sea surface height based on Topex altimeter measurements. Int. J. Rem. Sens. 17, 2647–2666.

Glazman, R.E., Fabrikant, A., Greysukh, A., 1996b. Nonlinear features of equatorial baroclinic Rossby waves detected in Topex altimeter observations. Nonlin. Proc. Geophys. 3, 115–126.

Hill, K.L., Robinson, I.S., Cipollini, P., 2000. Propagation characteristics of extratropical planetary waves observed in the ATSR global sea surface temperature record. J. Geophys. Res. 105 (C9), 21,927–21,946.

Jenkins, G.M., Watts, D.G., 1968. Spectral Analysis and its Applications. Holden-Day, San Francisco, p. 525.

Kang, Y.Q., Magaard, L., 1980. Annual baroclinic Rossby waves in the central north Pacific. J. Phys. Oceanogr. 10, 1159–1167.

Killworth, P.D., Blundell, J.R., 1999. The effect of bottom topography on the speed of long extratropical planetary waves. J. Phys. Oceanogr. 29, 2689–2710.

Killworth, P.D., Blundell, J.R., 2003. Long extratropical planetary wave propagation in the presence of slowly varying mean flow and bottom topography. Part I. The local problem, pp. 784–801; Part II. Ray propagation and comparison with observations, 33 (3), 802–821.

Killworth, P.D., Chelton, D.B., de Szoeke, R., 1997. The speed of observed and theoretical long extra-tropical planetary waves. J. Phys. Oceanogr. 27, 1946–1966.

LeBlond, P.H., Mysak, L.A., 1978. Waves in the Ocean. Elsevier, New York, p. 602.

Monin, A., Yaglom, A., 1980. Statistical Fluid Mechanics. MIT Press, Cambridge, MA.

Pedlosky, J., 1979. Geophysical Fluid Dynamics. Springer-Verlag, New York, p. 624.

Perigaud, C., Delecluse, P., 1992. Annual sea level variations in the southern tropical Indian Ocean from Geosat and shallow-water simulation. J. Geophys. Res. 97 (C12), 20169–20178.

Phillips, O.M., 1977. The Dynamics of the Upper Ocean. Cambridge University Press.

Price, J.M., Magaard, L., 1980. Rossby wave analysis of the baroclinic potential energy in the upper 500 m of the North Pacific. J. Mar. Res. 38, 249–264.

Qiu, B., Miao, W., Müller, P., 1997. Propagation and decay of forced and free baroclinic Rossby waves in off-equatorial oceans. J. Phys. Oceanogr. 27, 2405–2417.

Reznik, G.M., Tsybaneva, T.B., 1994. On the influence of ocean topography and stratification on planetary waves in the ocean (a two-layer model). Oceanology 34 (1), 5–14.

Schopf, P.S., Anderson, D.L.T., Smith, R., 1981. Beta-dispersion of low-frequency Rossby waves. Dyn. Atm. Oceans 5, 187–214.

Taileux, R., 2003. Comments on "the effect of bottom topography on the speed of long extratropical planetary waves". J. Phys. Oceanogr. 33, 1536–1542.

Tailleux, R., McWilliams, J.C., 2002. Energy propagation of long extratropical Rossby waves over slowly varying zonal topography. J. Fluid Mech. 473, 295–319.

Uz, B.M., Yoder, J.A., Osychny, V., 2001. Pumping of nutrients to ocean surface waters by the action of propagating planetary waves. Nature 409, 597–600.

Wang, L., Koblinsky, C.J., 1994. Influence of mid-ocean ridges on Rossby waves. J. Geophys. Res. 99 (C12), 25,143–25,153.

Weichman, P.B., Glazman, R.E., 2002. Spatial variations of a passive tracer in a random wave field. J. Fluid Mech. 453, 263–287.

Witham, G.B., 1974. Linear and Nonlinear Waves. Wiley and Sons, p. 365.